Time scales in the primary and secondary compression of soils

Yingxiao Liu[1] · Ronaldo I. Borja[1,*]

[1]Department of Civil and Environmental Engineering, Stanford University, Stanford, CA 94305, USA. *E-mail: borja@stanford.edu

Summary. The last several decades have seen a surge of papers dealing with analytical and semi-analytical solutions to the problem of one-dimensional consolidation of soils. But rarely has any of these contributions focused on the time scales arising from combined primary and secondary compression. Primary compression has always been attributed to the dissipation of excess pore pressure as fluid is expelled from the soil skeleton to the drainage boundaries. However, there have been several schools of thought when it comes to the process governing the secondary compression. In this paper, we attribute the secondary compression to any of the following processes occurring either individually or in combination: (a) rate-dependent (viscoplastic) constitutive response of the soil skeleton; (b) existence of a secondary pore scale system that expels fluid from the smaller-scale pores to the larger-scale pores; and (c) delayed compression due to creep following Bjerrum's concept of secondary consolidation. Contributions of the present work include closed-form analytical solutions to the problem of combined primary and secondary compression of soils in one dimension, as well as a quantitative analysis of the time scales involved in such coupled hydromechanical processes.

Keywords. Consolidation, creep, double porosity, primary and secondary compression, time scale, viscoplasticity

1 Introduction

Significant advances in the modeling of the stress-strain-time behavior of geomaterials have been made in the last several decades. Most works have revolved around clay because of its tendency to exhibit time-dependent responses. However, coarse-grained materials such as sand can also show time-dependent responses especially when they are mixed with fine-grained materials, organics, and water.

The best understood theory governing the time-dependent flow process in soils is the one-dimensional consolidation theory of Terzaghi. This theory as well as its variations have dominated the literature in the past several decades.

In the context of one-dimensional deformation and flow processes, some major improvements on the theory have been made taking into consideration the effect of partial saturation [20, 30, 37, 47, 49, 50, 56, 60, 87, 89], time-dependent surface loading [3, 31, 51, 57, 71, 73, 73, 76], layered soil systems [10, 43, 52, 62, 65, 75, 77], and simple nonlinearity including plasticity [58, 78, 82, 90] and varying compressibility and permeabilitiy [27, 39, 40, 61, 64, 75], among others. Even though the 1D kinematics have imposed limits on the applicability of these theories, they are still valuable contributions to the literature because they can be represented with closed-form analytical solutions.

However, it is also generally recognized that time-dependent deformation behavior of soils cannot be attributed to Terzaghi's consolidation theory alone. Terzaghi's theory states that the time-dependent deformation behavior of soil is due to the gradual transfer of stress from excess pore pressure to the effective stress as water is expelled from the pores. But continuing deformation in soil under a constant effective stress, also known as creep [17, 18, 41, 54, 67], has been observed after the excess pore pressure has fully dissipated or even in the absence of water [26, 29, 35, 72]. It is thus common to attribute the time-dependent deformation of soil to two processes: primary compression described by the Terzaghi theory and secondary compression representing additional deformation beyond the primary compression.

Secondary compression in soils is usually represented via rheological models [5, 7, 32, 46, 53, 70, 79, 88] or phenomenological relations between strain, stress, and time [8, 44, 55, 66]. Among them, Bjerrum [8] proposed a phenomenological model via a set of parallel straight lines on the void ratio-logarithm of effective vertical stress plane, where each line represents a certain duration of sustained loading. During the secondary compression stage, the void ratio of the soil decreases linearly with the logarithm of time under a constant effective vertical stress. Despite its wide use, Bjerrum's theory is faced with certain limitations as it predicts a compression increasing indefinitely with time under a constant effective stress, in contradiction with actual behavior that secondary consolidation does not persist indefinitely [2, 36]. Furthermore, an 'anomalous' behavior has been reported for some soils in which the secondary compression exhibits a nonlinear relation in the form of an S-shaped curve with logarithm of time [2, 25, 33, 36].

The mechanisms underlying the secondary compression is not yet well understood. Several theories include the fact that it arises from the viscous interaction of the solid surface with the adsorbed water [4, 68, 81], and/or interparticle sliding or rotation that evolves with time [19, 42], and/or physicochemical interaction of the electric double layers formed on the clay particles [9, 69]. Another school of thought attributes the secondary compression to the existence of two levels of pore sizes in the soil [23, 45, 48, 74], in which water is discharged from the smaller-scale pores to the larger-scale pores, a process that occurs at a much slower rate compared to the rate of primary compression [6, 28, 81].

The consolidation of soil is of complex nature involving multiple hydromechanical processes, and a better understanding of the time scale associated with each process enables us to predict the duration and to separate effects of different processes over the time domain. These time scales can be determined from the simple geometry and basic hydromechanical properties of soil, and collectively carry sufficient information to estimate the start and end of all stages of compression. Therefore, they play a significant role in the prediction of the long-term behavior of ground settlement in engineering practice with limited experimental data.

This paper focuses on the one-dimensional compression of soil with combined primary and secondary compression. We derive closed-form analytical solutions that accommodate for different secondary compression processes, including the viscoplastic rheological response of the soil skeleton, discharge of pore fluid from smaller-scale pores in a dual porosity system, and delayed compression of soil under Bjerrum's theory of secondary consolidation. The characteristic time scales involved in each case are identified mathematically. Quantitative studies are also conducted on how the time-dependence of the solutions are determined by the different time scales taken collectively.

2 Elasto-viscoplastic consolidation

We first consider the one-dimensional consolidation problem shown in Figure 1, where one layer of saturated soil of thickness H is subjected to a uniformly distributed pressure q on top. The bottom of the layer is impervious with no flux in or out, and is also constrained from vertical displacement, while the top surface is at zero pressure allowing water to drain freely. For the sign convention, the downward z direction is taken as positive and so is tension. The layer is assumed to deform elasto-viscoplastically and modeled by the simple frictional-link and dashpot system shown in Figure 2, where D is the constrained elastic modulus of the spring and $\mathcal{H}$ is the constrained plastic modulus of the link. The setup readily reduces to a Maxwell viscoelastic model when the initial yield stress σ_0 and plastic modulus $\mathcal{H}$ are both zero [34, 63]; however, it does not reduce to the Kelvin arrangement [1, 34, 38]. The plastic modulus $\mathcal{H}$ can be made to be a nonlinear function of deformation to closely match real soil behavior [14], but for now we shall assume it to be constant. In terms of the effective vertical stress σ'_{v}, the viscoplastic vertical strain rate is given by the Perzyna over-stress model [12, 59, 80] as

$$\dot{\varepsilon}_{\mathrm{v}}^{\mathrm{vp}} = \frac{f}{\eta}\mathrm{sign}(\sigma'_{\mathrm{v}})\,, \tag{1}$$

where η is the dashpot coefficient and f is the yield function given by

$$f = \sigma'_{\mathrm{v}} - \sigma_{\mathrm{Y}}\,. \tag{2}$$

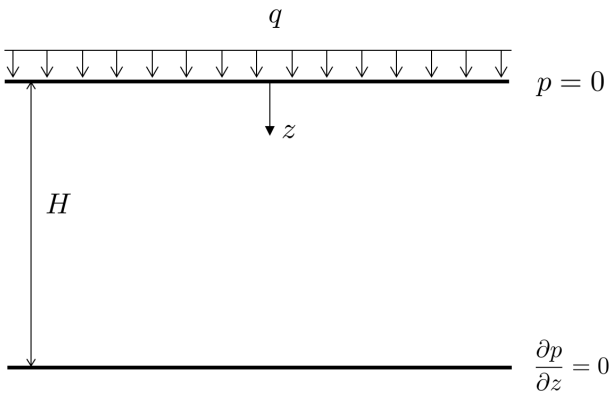

Fig. 1. Problem description

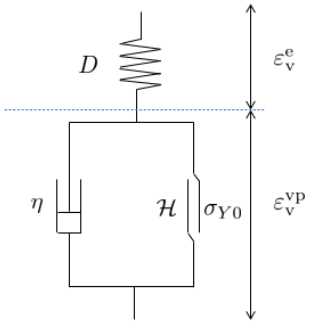

Fig. 2. Elasto-viscoplastic model

We consider a simple linear hardening given by

$$\sigma_{\mathrm{Y}} = \sigma_{\mathrm{Y0}} + \mathcal{H}\varepsilon_{\mathrm{v}}^{\mathrm{vp}}\,. \tag{3}$$

We also assume that the material is yielding throughout the process, so we set $\sigma_{\mathrm{Y0}} = 0$. Thus,

$$\dot{\varepsilon}_{\mathrm{v}}^{\mathrm{vp}} = \frac{\sigma_{\mathrm{v}}' - \mathcal{H}\varepsilon_{\mathrm{v}}^{\mathrm{vp}}}{\eta}. \tag{4}$$

Solving the above differential equation, we obtain a closed form solution for the viscoplastic strain as

$$\varepsilon_{\mathrm{v}}^{\mathrm{vp}} = \int_0^t \frac{\sigma_{\mathrm{v}}'}{\eta} e^{-\mathcal{H}(t-\tau)/\eta} \mathrm{d}\tau. \tag{5}$$

The relation between the total vertical strain and the effective vertical stress can be expressed as

$$\varepsilon_{\mathrm{v}} = \varepsilon_{\mathrm{v}}^{\mathrm{e}} + \varepsilon_{\mathrm{v}}^{\mathrm{vp}} = \frac{\sigma'_{\mathrm{v}}}{D} + \int_0^t \frac{\sigma'_{\mathrm{v}}}{\eta} e^{-\mathcal{H}(t-\tau)/\eta} \mathrm{d}\tau \,, \tag{6}$$

from which the corresponding strain rate is derived as

$$\dot{\varepsilon}_{\mathrm{v}} = \frac{\dot{\sigma}'_{\mathrm{v}}}{D} + \frac{\sigma'_{\mathrm{v}}}{\eta} - \frac{\mathcal{H}}{\eta} \int_0^t \frac{\sigma'_{\mathrm{v}}}{\eta} e^{-\mathcal{H}(t-\tau)/\eta} \mathrm{d}\tau \,. \tag{7}$$

The above strain rate equation has a form similar to the one developed by Xie et al. [76] for a viscoelastic soil model.

We make the following additional assumptions similar to those adopted in the derivation of Terzaghi's one-dimensional consolidation theory: (a) the solid grain and fluid are both incompressible, and (b) deformation in the soil skeleton is infinitesimal. Under these assumptions, the volumetric change in the solid due to compression is simply equal to the amount of fluid coming in/out of the pore space. The strong form of the boundary-value problem is stated as follows: Find the vertical displacement u of the soil skeleton and excess fluid pressure p such that, for $0 < z < H$,

$$\left.\begin{aligned} \frac{\partial \sigma'_{\mathrm{v}}}{\partial z} - \frac{\partial p}{\partial z} &= 0 \\ \dot{\varepsilon}_{\mathrm{v}} - \frac{k}{\rho_{\mathrm{w}} g} \frac{\partial^2 p}{\partial z^2} &= 0 \end{aligned}\right\} , \tag{8}$$

subject to boundary and initial conditions

$$\left.\begin{aligned} p(z=0,t) &= 0 \\ \frac{\partial p}{\partial z}\Big|_{z=H,t} &= 0 \\ \sigma'_{\mathrm{v}}(z,t=0) &= 0 \\ p(z>0,t=0) &= q \end{aligned}\right\} , \tag{9}$$

where p is the excess pore water pressure, ρ_{w} is the mass density of fluid, g is the gravity acceleration constant, and k is the hydraulic conductivity of the soil. Substituting the constitutive equation relating σ'_{v} and ε_{v}, we obtain

$$c_{\mathrm{v}} \frac{\partial^2 p}{\partial z^2} - \frac{\partial p}{\partial t} - \frac{D}{\eta} \int_0^t \frac{\partial p}{\partial \tau} e^{-\mathcal{H}(t-\tau)/\eta} \mathrm{d}\tau = 0 \,, \tag{10}$$

where

$$c_{\mathrm{v}} = \frac{kD}{\rho_{\mathrm{w}} g} \tag{11}$$

is the coefficient of consolidation.

The problem can be solved by separation of variables, followed by Laplace transformation adopted in [76]. First, we assume that $p(z,t) = Z(z)T(t)$,

and substitute this expression back into Equation (10) to obtain an ordinary differential equation (ODE) of the form

$$Z'' + \lambda^2 Z = 0\,, \tag{12}$$

where λ is some undetermined coefficient. The general solution to Z is of the form

$$Z = a_1 \cos \lambda z + a_2 \sin \lambda z\,. \tag{13}$$

Using the two boundary conditions $Z(0) = 0$ and $Z'(H) = 0$, we find

$$a_1 = 0 \tag{14}$$

and

$$\lambda_m = \frac{2m-1}{2H}\pi, \quad m = 1, 2, 3\ldots \tag{15}$$

Therefore, any arbitrary function of excess pore water pressure can be expressed as

$$p(z,t) = \sum_{m=1}^{\infty} T_m(t) \sin\left(\frac{M}{H} z\right), \tag{16}$$

with $M = (2m-1)\pi/2$. Substituting $p(z,t)$ into Equation (10), we obtain another ODE for the variable t of the form

$$c_{\mathrm{v}} \frac{M^2}{H^2} T_m(t) + T'_m(t) + \frac{D}{\eta} \int_0^t T'_m(\tau) e^{-\mathcal{H}(t-\tau)/\eta} \mathrm{d}\tau = 0\,. \tag{17}$$

The initial value of T_m can be derived from the condition

$$p(t=0) = q = \sum_{m=1}^{\infty} \frac{2q}{M} \sin \frac{M}{H} z \tag{18}$$

as $T_m(0) = 2q/M$. Performing the Laplace transformation on the ODE and letting $F_m(s) = \mathscr{L}(T_m(t))$, we get

$$c_{\mathrm{v}} \frac{M^2}{H^2} F_m(s) + \left(sF_m(s) - \frac{2q}{M}\right) + \frac{D}{\eta}\left(sF_m(s) - \frac{2q}{M}\right) \frac{1}{s + \mathcal{H}/\eta} = 0\,. \tag{19}$$

Before solving for the explicit form of $F_m(s)$, we first define three terms representing different characteristic time scales for this problem:

$$\tau_{\mathrm{h}} = \frac{H^2}{c_{\mathrm{v}}} \tag{20}$$

related to primary compression, where c_{v} is the coefficient of consolidation defined in Equation (11), and two terms,

$$\tau_{\mathrm{v1}} = \frac{\eta}{\mathcal{H}} \tag{21}$$

and

$$\tau_{\mathrm{v}2} = \frac{\eta}{D + \mathcal{H}} \tag{22}$$

related to secondary compression attributed to viscoplastic deformation. Then, the solution of $F_m(s)$ can be expressed in terms of these three characteristic time scales as

$$\begin{aligned} F_m(s) &= \frac{2q}{M} \frac{s + 1/\tau_{\mathrm{v}2}}{s^2 + (1/\tau_{\mathrm{v}2} + M^2/\tau_{\mathrm{h}})s + M^2/\tau_{\mathrm{h}}\tau_{\mathrm{v}1}} \\ &= \frac{2q}{M}\Big(\frac{r_{m1}}{s - s_{m1}} + \frac{r_{m2}}{s - s_{m2}}\Big), \end{aligned} \tag{23}$$

with

$$\left.\begin{aligned} s_{m1} &= -\frac{1}{2}\left[\Big(\frac{1}{\tau_{\mathrm{v}2}} + \frac{M^2}{\tau_{\mathrm{h}}}\Big) - \sqrt{\Big(\frac{1}{\tau_{\mathrm{v}2}} + \frac{M^2}{\tau_{\mathrm{h}}}\Big)^2 - \frac{4M^2}{\tau_{\mathrm{h}}\tau_{\mathrm{v}1}}}\,\right] \\ s_{m2} &= -\frac{1}{2}\left[\Big(\frac{1}{\tau_{\mathrm{v}2}} + \frac{M^2}{\tau_{\mathrm{h}}}\Big) + \sqrt{\Big(\frac{1}{\tau_{\mathrm{v}2}} + \frac{M^2}{\tau_{\mathrm{h}}}\Big)^2 - \frac{4M^2}{\tau_{\mathrm{h}}\tau_{\mathrm{v}1}}}\,\right] \\ r_{m1} &= \frac{M^2/\tau_{\mathrm{h}} + s_{m2}}{s_{m2} - s_{m1}} \\ r_{m2} &= \frac{M^2/\tau_{\mathrm{h}} + s_{m1}}{s_{m1} - s_{m2}} \end{aligned}\right\}. \tag{24}$$

The time function can then be calculated by inverse Laplace transformation [22] as

$$T_m(t) = \frac{2q}{M}\Big(r_{m1}e^{s_{m1}t} + r_{m2}e^{s_{m2}t}\Big), \tag{25}$$

which gives the final expression for the excess pore pressure as

$$p(z,t) = \sum_{m=1}^{\infty} \frac{2q}{M} \sin\big(\frac{M}{H}z\big)\Big(r_{m1}e^{s_{m1}t} + r_{m2}e^{s_{m2}t}\Big). \tag{26}$$

Substituting the equation into the expression for strain, we obtain

$$\varepsilon_{\mathrm{v}}(z,t) = -\frac{q}{E} - \frac{q}{\mathcal{H}}(1 - e^{-\mathcal{H}t/\eta}) + \sum_{m=1}^{\infty} \frac{2q}{M} \sin\big(\frac{M}{H}z\big) g_m(t), \tag{27}$$

where

$$\begin{aligned} g_m(t) = \frac{r_{m1}e^{s_{m1}t} + r_{m2}e^{s_{m2}t}}{D} &+ \frac{r_{m1}}{\mathcal{H} + s_{m1}\eta}(e^{s_{m1}t} - e^{-\mathcal{H}t/\eta}) \\ &+ \frac{r_{m2}}{\mathcal{H} + s_{m2}\eta}(e^{s_{m2}t} - e^{-\mathcal{H}t/\eta}). \end{aligned}$$

The normalized settlement can be calculated by taking the integral of $-\varepsilon_{\mathrm{v}}$ over the whole depth and then dividing the result by the thickness of the soil layer H. The final result is

$$\frac{\Delta H(t)}{H} = \frac{q}{D} + \frac{q}{\mathcal{H}}(1 - e^{-\mathcal{H}t/\eta}) - \sum_{m=1}^{\infty} \frac{2q}{M^2}(1 - \cos M) g_m(t)\,. \tag{28}$$

The first term of the solution depends only on the elastic modulus of the soil and determines the elastic component of the strain in the consolidating layer. The second term depends only on the viscoplastic parameters, which can be treated as the uncoupled portion of the viscoplastic strain. The third term, where all mechanical parameters enter together with the hydraulic conductivity, gives the combined effects of primary and secondary compression. Both the second and the third terms are time-dependent.

It can be observed that the two parameters η and k, which contain time in their dimensions, only appear in the three characteristic time scales defined before, namely, τ_{h}, τ_{v1}, and τ_{v2}. Therefore, the relative magnitudes of these time scales completely determine the time-dependent components of the solution. We shall elaborate these three time scales with numerical examples in the sections below. In the numerical examples, we assume the following parameters: surface load $q = 10$ kPa, thickness of soil layer $H = 10$ m, and viscosity of the soil $\eta = 10^{10}$ kPa $\cdot$ s.

2.1 Effect of τ_{v1} versus τ_{v2}

In this example, τ_{h} and τ_{v1} were fixed at 10^2 s and 10^5 s, respectively, while the ratio

$$c_1 = \frac{\tau_{\mathrm{v2}}}{\tau_{\mathrm{v1}}} = \frac{\mathcal{H}}{D + \mathcal{H}} \tag{29}$$

was made to vary between 0 and 1 depending on the value of τ_{v2}.

Figure 3 shows how the relative magnitude of τ_{v1} and τ_{v2} changes the shape of the settlement-time curves. The ratio between the current settlement and the final settlement when time approaches infinity, $\bar{U} = \Delta H(t)/\Delta H_{\mathrm{ult}}$, also known as the average degree of consolidation, is plotted against time in log scale. The vertical axis is presented in the reverse order to ensure that the resulting curves are consistent with those used in engineering practice.

Apart from the two limiting cases where c_1 is equal to 0 or 1, all curves show a double S-shaped variation representing a separation of two different settlement stages across different time scales. Such a separation is most obvious when c_1 is close to 0.5. The first S-shaped curve represents the first stage of settlement, which occurs after the surface load is applied and concludes at around 200 s. Thereafter, a plateau forms on these curves representing the transition from the first settlement stage to the second stage. This is followed by a second settlement stage and a second S-shaped variation on the semi-log plot.

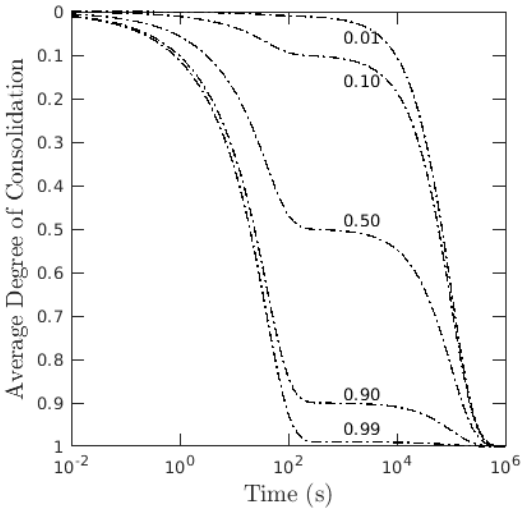

Fig. 3. Variation of average degree of consolidation $\bar{U}$ with c_1.

If the two settlement stages are interpreted as "primary" and "secondary" stages, it can be inferred that only the primary stage can be observed for $c_1 = 1$ while only the secondary stage can be observed for $c_1 = 0$. As c_1 increases from 0 to 1, the curve changes from a long-tail double-S curve where the secondary stage is dominant to a curve where the primary stage is dominant. All curves merge to the same point at a time instant that lies somewhere between 10^5 s and 10^6 s when the whole settlement process has concluded, which is on the same order of magnitude as $\tau_{\mathrm{v}1}$. In addition, the primary settlement stage for all curves concludes nearly simultaneously at around 100 s, which is approximately equal to τ_{h}. Incidentally, this is also the same time instant when the ground settlement has concluded for the limiting case when $c_1 = 1$, where only the primary settlement can be observed. Therefore, τ_{h} and $\tau_{\mathrm{v}1}$ can be interpreted as the durations of the primary settlement stage and the entire settlement process, respectively.

The coefficient c_1 can also be provided with a physical meaning. If the presence of fluid was excluded in this problem, the instantaneous settlement would be equal to q/D while the final settlement when time approaches infinity would be equal to $q/D + q/\mathcal{H}$, and the ratio between these two values would be equal to c_1. If fluid was included, we would have time-dependent primary and secondary stages instead, but c_1 still represents the ratio between the settlements that would occur in the primary stage and the whole process, as shown in Figure 3. Therefore, with two different settlement stages considered, the primary stage would be more closely related to the hydrodynamically damped elastic deformation of the soil, while the effect of viscoplasticity would become significant in the secondary stage.

We should note that the above analysis is based on the condition that both τ_{v1} and τ_{v2} are greater than τ_h, which implies that the fluid dissipation occurs faster compared to the viscoplastic deformation of the soil.

2.2 Effect of τ_{v1} versus τ_h

In the second example, τ_{v1} and τ_{v2} were fixed at 10^8 s and 5×10^7 s, resulting in $c_1 = 0.5$. Based on the analysis from the previous section, the primary settlement would have the same magnitude as the secondary settlement. Different τ_h values, ranging from 10^5 s to 10^{10} s, were analyzed by varying the hydraulic conductivity k, and the resulting curves are plotted in Figure 4. For convenience, we define a second coefficient c_2 as

$$c_2 = \frac{\tau_h}{\tau_{v1}} = \frac{H^2}{c_v}\frac{\mathcal{H}}{\eta} \tag{30}$$

to represent the ratio between the time scales for the pressure dissipation and the viscoplastic deformation of the soil. Since τ_h and τ_{v1} together determine the duration of different settlement stages, the shape of the curve would be affected by different c_2 values.

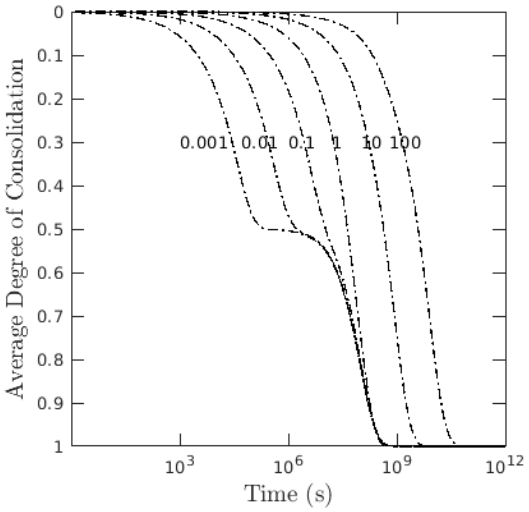

Fig. 4. Variation of average degree of consolidation with c_2.

As shown in Figure 4, the case when c_2 is smaller than 1 produces double S-shaped curves and is similar to the case presented before. All curves end at the same time instant determined by τ_{v1}. The whole settlement process takes the same amount of time to finish regardless of the values of hydraulic

conductivity k. When c_2 is very small (less than 0.01), primary settlement develops very fast compared with the secondary settlement, and a separation of the two settlement stages can be clearly seen. A transition region, shown as a plateau on the curve, is very distinct, and its duration is determined by the coefficient c_2: the smaller the c_2, the greater the difference between $\tau_{\mathrm{v}1}$ and τ_{h}, resulting in a more distinct separation of time scales. We also see that the shape of the second S curve, representing the secondary settlement, is insensitive to the value of the hydraulic conductivity, which implies that the hydrodynamic effect is negligible during the viscoplastic deformation stage.

As c_2 becomes larger, the first S curve shifts to the right while the second S curve remains fixed. When $c_2 = 0.1$, which means τ_{h} is only one order of magnitude smaller than $\tau_{\mathrm{v}1}$, the first S curve shifts to the right by a distance that is enough for it to be smoothly connected to the second S curve, and from then on the separation of the two curves is no longer evident. As c_2 increases further to 1, the first S curve begins to cover the second S curve. Up to this point the duration of the whole settlement process remains unchanged, being approximately equal to $\tau_{\mathrm{v}1}$. Finally, as c_2 increases beyond the value 1, the primary settlement becomes the more dominant process and τ_{h} becomes the more dominant time scale. The duration of the total settlement is now determined solely by τ_{h}, and varying the hydraulic conductivity values simply results in a series of parallel curves in which the effect of viscoplasticity is no longer evident.

2.3 Summary of main points

For a one-dimensional system in which the primary compression is attributed to pore pressure dissipation and the secondary compression is attributed to viscoplastic deformation of the soil skeleton, the shape of the settlement-time curve is determined by three characteristic time scales represented by τ_{h}, $\tau_{\mathrm{v}1}$, and $\tau_{\mathrm{v}2}$. The duration of the compression process is determined by the larger of τ_{h} and $\tau_{\mathrm{v}1}$: If $\tau_{\mathrm{h}} > \tau_{\mathrm{v}1}$, only one settlement stage would form, whereas if $\tau_{\mathrm{h}} < \tau_{\mathrm{v}1}$, both the primary and secondary settlement stages would manifest themselves on the settlement-time curves. The time scale τ_{h} determines the duration of the primary compression stage, whereas the time scale $\tau_{\mathrm{v}1}$ determines the duration of the secondary compression stage. The relative values of $\tau_{\mathrm{v}1}$ and $\tau_{\mathrm{v}2}$ determine the shape of the resulting settlement-time response curves, which can be either in the form of a single S-shaped curve or a double S-shaped curve.

The results presented above are supported by field observations. Chang et al. [21] reported an unexpected result of a survey at the Gulf of Mexico shale gas reservoir in which two different land subsidence rates were observed, the second one being recorded after the production has ceased. They postulated a multi-layer model consisting of permeable sand and impermeable viscous shale layers to explain the two subsidence rates. However, the results of this study suggest that the two subsidence rates can also be explained with a

single saturated viscoplastic shale layer experiencing combined primary and secondary compression.

3 Double porosity consolidation

It is generally recognized that natural geomaterials can exhibit two distinct porosity scales. In fissured rocks, the two pore scales can be represented by the micro-fracture pores and the matrix pores [83, 84]; in aggregated soils they can be represented by the inter-aggregate pores and intra-aggregate pores [13, 15, 24, 85]. In this section, we shall call the larger-scale pores as the "macropores" and the smaller-scale pores as the "micropores." Fluid flow mechanisms considered in the following discussions include flow through the macropores, flow through the micropores, and fluid mass exchanges between the macropores and micropores.

From here on, we shall dispense with the assumption of incompressible solid grains and fluids and consider both of them to be compressible. Consequently, both fluid density and porosity can vary with the pore pressure. Let ψ_1 and ψ_2 denote the pore fractions occupied by the micropores and macropores, respectively, which satisfy the closure condition $\psi_1 + \psi_2 = 1$. Denoting the excess fluid pressure at the macropores and micropores as p_1 and p_2, respectively, the balance of fluid mass in the macropores and micropores takes the form

$$\frac{\dot{p}_1}{m_1} + \beta_1 \nabla \cdot \dot{\boldsymbol{u}} = -\nabla \cdot \boldsymbol{q}_1 + c_1 \,, \tag{31}$$

$$\frac{\dot{p}_2}{m_2} + \beta_2 \nabla \cdot \dot{\boldsymbol{u}} = -\nabla \cdot \boldsymbol{q}_2 + c_2 \,, \tag{32}$$

where $\boldsymbol{u}$ is the displacement vector of the soil skeleton; m_1 and m_2 are the Biot moduli [85, 86]; $\beta_1 = B\psi_1$ and $\beta_2 = B\psi_2$ are the products of the Biot coefficient B [11, 16] and pore fractions ψ_1 and ψ_2; $\boldsymbol{q}_1$ and $\boldsymbol{q}_2$ are the Darcy fluxes in the macropores and micropores, respectively; and c_1 and c_2 are the fluid mass transfer terms between the two pore scales.

Specializing now to the 1D case, we first define $\sigma'_{\rm v}$ as the effective vertical stress in a double-porosity medium using the expression developed by Borja and Koliji [15] as

$$\sigma'_{\rm v} = \sigma_{\rm v} + \beta_1 p_1 + \beta_2 p_2 \,, \tag{33}$$

where $\sigma_{\rm v}$ is the total vertical stress in the soil column. Furthermore, we assume Darcy's law in the macropores and micropores and write

$$q_1 = -k_1 \frac{\partial p_1}{\partial z} \,, \qquad q_2 = -k_2 \frac{\partial p_2}{\partial z} \,, \tag{34}$$

where k_1 and k_2 are the hydraulic conductivities in the macropores and micropores, respectively. Lastly, we assume that the fluid mass exchange rates are proportional to the pressure difference at the two pore scales,

$$c_1 = \kappa(p_2 - p_1) = -c_2\,. \tag{35}$$

We now state the strong form of the boundary-value problem: Find the vertical displacement u of the soil skeleton and excess fluid pressures p_1 and p_2 in the macropores and micropores, respectively, such that for $0 < z < H$,

$$\left.\begin{aligned} \frac{\partial(\sigma'_{\mathrm{v}} - \beta_1 p_1 - \beta_2 p_2)}{\partial z} &= 0 \\ \frac{\dot{p}_1}{m_1} + \beta_1 \dot{\varepsilon}_{\mathrm{v}} - \frac{k_1}{\rho_{\mathrm{w}} g}\frac{\partial^2 p_1}{\partial z^2} &= \kappa(p_2 - p_1) \\ \frac{\dot{p}_2}{m_2} + \beta_2 \dot{\varepsilon}_{\mathrm{v}} - \frac{k_2}{\rho_{\mathrm{w}} g}\frac{\partial^2 p_2}{\partial z^2} &= -\kappa(p_2 - p_1) \end{aligned}\right\}. \tag{36}$$

The first equation above is the equilibrium condition in the vertical direction, whereas the last two equations are the fluid mass balance equations in the macropores and micropores.

Before stating the boundary and initial conditions, we first note that the constrained 1D condition allows the displacement and fluid pressures to be uncoupled. This is facilitated by using the elasto-viscoplastic constitutive relation (7) to express σ'_{v} in terms of ϵ_{v} in the equilibrium condition, solving for ϵ_{v} in terms of p_1 and p_2, and substituting the result into the fluid mass balance conditions. The equivalent strong form then reads: Find p_1 and p_2 such that for $0 < z < H$,

$$\begin{aligned} N_1\dot{p}_1 + {\beta_1}^2\dot{p}_1 + \beta_1^2\frac{D}{\eta}\int_0^t \frac{\partial p_1}{\partial \tau}e^{-\mathcal{H}(t-\tau)/\eta}\mathrm{d}\tau + \beta_1\beta_2\frac{D}{\eta}\int_0^t \frac{\partial p_2}{\partial \tau}e^{-\mathcal{H}(t-\tau)/\eta}\mathrm{d}\tau \\ + \beta_1\beta_2\dot{p}_2 + \Big(\frac{\beta_1 C_1}{2} + \frac{\beta_2 C_2}{2} - 1\Big)\frac{q}{\eta}e^{-\mathcal{H}t} = c_{\mathrm{v}1}\frac{\partial^2 p_1}{\partial x^2} + \gamma(p_2 - p_1)\,; \end{aligned} \tag{37}$$

$$\begin{aligned} N_2\dot{p}_2 + {\beta_2}^2\dot{p}_2 + \beta_2^2\frac{D}{\eta}\int_0^t \frac{\partial p_2}{\partial \tau}e^{-\mathcal{H}(t-\tau)/\eta}\mathrm{d}\tau + \beta_1\beta_2\frac{D}{\eta}\int_0^t \frac{\partial p_1}{\partial \tau}e^{-\mathcal{H}(t-\tau)/\eta}\mathrm{d}\tau \\ + \beta_1\beta_2\dot{p}_1 + \Big(\frac{\beta_1 C_1}{2} + \frac{\beta_2 C_2}{2} - 1\Big)\frac{q}{\eta}e^{-\mathcal{H}t} = c_{\mathrm{v}2}\frac{\partial^2 p_2}{\partial x^2} - \gamma(p_2 - p_1)\,, \end{aligned} \tag{38}$$

with boundary and initial conditions

$$\left.\begin{aligned} \frac{\partial p_i}{\partial z}\Big|_{z=H,t} &= 0 \\ p_i(z, t=0) &= C_i q/2 \\ p_i(z=0, t) &= 0 \end{aligned}\right\} \text{ for } \; i = 1, 2\,, \tag{39}$$

where q is defined in Equation (9).

The coefficients introduced in the foregoing equations are defined as follows:

$$N_i = \frac{D}{m_i}\,, \qquad c_{\mathrm{v}i} = \frac{k_i D}{\rho_{\mathrm{w}} g}\,, \qquad i = 1, 2\,; \tag{40}$$

and $\gamma = \kappa D$. The other two coefficients C_1 and C_2 determine the initial excess pore pressures and are calculated from the fact that immediately after the load is applied, undrained condition prevails and the change in the fluid content in the pores must be equal to zero. Thus, the jump in the excess pore pressures satisfies the conditions

$$N_i \mathrm{d}p_i + \beta_i \mathrm{d}\sigma'_{\mathrm{v}} = 0, \qquad i = 1, 2 \tag{41}$$

and

$$\mathrm{d}\sigma'_{\mathrm{v}} = \beta_1 \mathrm{d}p_1 + \beta_2 \mathrm{d}p_1 - q\,, \tag{42}$$

from which we arrive at

$$\mathrm{d}p_1 = \frac{N_2\beta_1}{N_1N_2 + N_2\beta_1^2 + N_1\beta_2^2} q = \frac{C_1}{2} q\,, \tag{43}$$

$$\mathrm{d}p_2 = \frac{N_1\beta_2}{N_1N_2 + N_2\beta_1^2 + N_1\beta_2^2} q = \frac{C_1}{2} q\,. \tag{44}$$

We further use the coefficient C_3 to denote the negative of the coefficient before the term $qe^{-\mathcal{H}t}/\eta$ as

$$C_3 = 1 - \frac{\beta_1 C_1}{2} - \frac{\beta_2 C_2}{2} = \frac{N_1 N_2}{N_1N_2 + N_2\beta_1^2 + N_1\beta_2^2}\,. \tag{45}$$

Using the same techniques as before, we first separate the variables and express p_1 and p_2 as Fourier series as

$$p_1(z,t) = \sum_{m=1}^{\infty} A_m(t) \sin\left(\frac{M}{H} z\right), \tag{46}$$

$$p_2(z,t) = \sum_{m=1}^{\infty} B_m(t) \sin\left(\frac{M}{H} z\right), \tag{47}$$

with $M = (2m-1)\pi/2$. Substituting $p_1(z,t)$ and $p_2(z,t)$ into Equations (37) and (38), we obtain a system of ODEs in terms of $A_m(t)$ and $B_m(t)$ only:

$$\left(c_{\mathrm{v}1}\frac{M^2}{H^2} + \gamma\right) A_m(t) + (N_1 + \beta_1^2) A'_m(t) + \beta_1^2 \frac{D}{\eta} \int_0^t A'_m(\tau) e^{-\mathcal{H}(t-\tau)/\eta} \mathrm{d}\tau - \gamma$$
$$\cdot B_m(t) + \beta_1\beta_2 B'_m(t) + \beta_1\beta_2 \frac{D}{\eta} \int_0^t B'_m(\tau) e^{-\mathcal{H}(t-\tau)/\eta} \mathrm{d}\tau = 2C_3\beta_1 \frac{D}{\eta} \frac{q}{M} e^{-\mathcal{H}t/\eta}\,, \tag{48}$$

$$\left(c_{\mathrm{v}2}\frac{M^2}{H^2} + \gamma\right) B_m(t) + (N_2 + \beta_2^2) B'_m(t) + \beta_2^2 \frac{D}{\eta} \int_0^t B'_m(\tau) e^{-\mathcal{H}(t-\tau)/\eta} \mathrm{d}\tau - \gamma$$
$$\cdot A_m(t) + \beta_1\beta_2 A'_m(t) + \beta_1\beta_2 \frac{D}{\eta} \int_0^t A'_m(\tau) e^{-\mathcal{H}(t-\tau)/\eta} \mathrm{d}\tau = 2C_3\beta_2 \frac{D}{\eta} \frac{q}{M} e^{-\mathcal{H}t/\eta}\,, \tag{49}$$

with the initial solution

$$A_m(0) = \frac{C_1 q}{M}\,, \tag{50}$$

$$B_m(0) = \frac{C_2 q}{M}\,. \tag{51}$$

We next perform the Laplace transformation on these equation by defining $F_m(s) = \mathscr{L}(A_m(t))$ and $G_m(s) = \mathscr{L}(B_m(t))$, and then use the relation $\mathscr{L}(f'(t)) = s\mathscr{L}(f(t)) - f(0)$ to arrive at

$$\begin{aligned}
&\Big[c_{\mathrm{v}1}\frac{M^2}{H^2} + \gamma + (N_1+\beta_1^2)s + \beta_1^2\frac{Ds}{\eta s+\mathcal{H}}\Big]F_m(s)\\
&\qquad + \Big[-\gamma + \beta_1\beta_2 s + \beta_1\beta_2\frac{Ds}{\eta s+\mathcal{H}}\Big]G_m(s)\\
&= \Big[C_1(N_1+\beta_1^2) + C_2\beta_1\beta_2 + \beta_1(C_1\beta_1 + C_2\beta_2 + 2C_3)\frac{D}{\eta s+\mathcal{H}}\Big]\frac{q}{M}\,, \qquad (52)\\
&\qquad \Big[-\gamma + \beta_1\beta_2 s + \beta_1\beta_2\frac{Ds}{\eta s+\mathcal{H}}\Big]F_m(s)\\
&\qquad + \Big[c_{\mathrm{v}2}\frac{M^2}{H^2} + \gamma + (N_2+\beta_2^2)s + \beta_2^2\frac{Ds}{\eta s+\mathcal{H}}\Big]G_m(s)\\
&= \Big[C_2(N_2+\beta_2^2) + C_1\beta_1\beta_2 + \beta_2(C_1\beta_1 + C_2\beta_2 + 2C_3)\frac{D}{\eta s+\mathcal{H}}\Big]\frac{q}{M}\,. \qquad (53)
\end{aligned}$$

To simplify the final expression, we define four characteristic time scales

$$\tau_{\mathrm{h}}^a = \frac{H^2}{c_{\mathrm{v}1}}\,, \quad \tau_{\mathrm{h}}^b = \frac{H^2}{c_{\mathrm{v}2}}\,, \quad \tau_{\mathrm{v}1} = \frac{\eta}{\mathcal{H}}\,, \quad \tau_{\mathrm{v}2} = \frac{\eta}{D}\,, \tag{54}$$

and several other terms

$$\mathcal{M}_1 = N_1 N_2 + N_1 \beta_2^2 + N_2 \beta_1^2 \,, \tag{55}$$

$$\mathcal{M}_2 = \Big(\frac{M^2}{\tau_{\rm h}^a} + \gamma\Big)(N_2 + \beta_2^2) + \Big(\frac{M^2}{\tau_{\rm h}^b} + \gamma\Big)(N_1 + \beta_1^2) + 2\gamma\beta_1\beta_2 \,, \tag{56}$$

$$\mathcal{M}_3 = \frac{M^4}{\tau_{\rm h}^a \tau_{\rm h}^b} + \gamma M^2 \Big(\frac{1}{\tau_{\rm h}^a} + \frac{1}{\tau_{\rm h}^b}\Big) \,, \tag{57}$$

$$\mathcal{M}_4 = \frac{M^2}{\tau_{\rm h}^a}\beta_2^2 + \frac{M^2}{\tau_{\rm h}^b}\beta_1^2 + \gamma(\beta_1 + \beta_2)^2 \,, \tag{58}$$

$$\mathcal{M}_5 = N_1 \beta_2^2 + N_2 \beta_1^2 \,, \tag{59}$$

$$\mathcal{M}_6 = \frac{\mathcal{M}_1}{\tau_{\rm v1}} + \mathcal{M}_2 + \frac{\mathcal{M}_5}{\tau_{\rm v2}} \,, \tag{60}$$

$$\mathcal{M}_7 = \frac{\mathcal{M}_2}{\tau_{\rm v1}} + \mathcal{M}_3 + \frac{\mathcal{M}_4}{\tau_{\rm v2}} \,, \tag{61}$$

$$\begin{aligned}\mathcal{M}_8^a = {} & [C_1(N_1 + \beta_1^2) + C_2\beta_1\beta_2]\frac{M^2}{\tau_{\rm h}^b} \\ & + \gamma[C_1(N_1 + \beta_1^2) + C_2(N_2 + \beta_2^2) + (C_1 + C_2)\beta_1\beta_2] \,,\end{aligned} \tag{62}$$

$$\begin{aligned}\mathcal{M}_8^b = {} & [C_2(N_2 + \beta_2^2) + C_1\beta_1\beta_2]\frac{M^2}{\tau_{\rm h}^a} \\ & + \gamma[C_1(N_1 + \beta_1^2) + C_2(N_2 + \beta_2^2) + (C_1 + C_2)\beta_1\beta_2] \,,\end{aligned} \tag{63}$$

$$\mathcal{M}_9^a = \Big[\frac{M^2}{\tau_{\rm h}^b}\beta_1 + \gamma(\beta_1 + \beta_2)\Big](C_1\beta_1 + C_2\beta_2 + 2C_3) \,, \tag{64}$$

$$\mathcal{M}_9^b = \Big[\frac{M^2}{\tau_{\rm h}^a}\beta_2 + \gamma(\beta_1 + \beta_2)\Big](C_1\beta_1 + C_2\beta_2 + 2C_3) \,, \tag{65}$$

$$\mathcal{M}_{10}^a = \frac{C_1\mathcal{M}_1}{\tau_{\rm v1}} + \frac{C_1\mathcal{M}_5 + 2C_3N_2\beta_1}{\tau_{\rm v2}} + \mathcal{M}_8^a \,, \tag{66}$$

$$\mathcal{M}_{10}^b = \frac{C_2\mathcal{M}_1}{\tau_{\rm v1}} + \frac{C_2\mathcal{M}_5 + 2C_3N_1\beta_2}{\tau_{\rm v2}} + \mathcal{M}_8^b \,, \tag{67}$$

$$\mathcal{M}_{11}^a = \frac{\mathcal{M}_8^a}{\tau_{\rm v1}} + \frac{\mathcal{M}_9^a}{\tau_{\rm v2}} \,, \tag{68}$$

$$\mathcal{M}_{11}^b = \frac{\mathcal{M}_8^b}{\tau_{\rm v1}} + \frac{\mathcal{M}_9^b}{\tau_{\rm v2}} \,, \tag{69}$$

and solve for $F_m(s)$ and $G_m(s)$ as

$$F_m(s) = \frac{q}{M}\frac{C_1\mathcal{M}_1 s^2 + \mathcal{M}_{10}^a s + \mathcal{M}_{11}^a}{\mathcal{M}_1 s^3 + \mathcal{M}_6 s^2 + \mathcal{M}_7 s + \mathcal{M}_3/\tau_{\rm v1}} \,, \tag{70}$$

$$G_m(s) = \frac{q}{M}\frac{C_2\mathcal{M}_1 s^2 + \mathcal{M}_{10}^b s + \mathcal{M}_{11}^b}{\mathcal{M}_1 s^3 + \mathcal{M}_6 s^2 + \mathcal{M}_7 s + \mathcal{M}_3/\tau_{\rm v1}} \,. \tag{71}$$

For the special case where $N_1 = N_2 = 0$, the resulting $\mathcal{M}_1$ is zero and we obtain a second order polynomial in the denominator and a first order

polynomial in the numerator. In this case, the solution has the form similar to what we have derived in Equation (23) and will not be repeated here. For the general case where $\mathcal{M}_1$ is not zero, the solution can be formulated as

$$F_m(s) = \frac{q}{M}\Big(\frac{r^a_{m1}}{s-s_{m1}} + \frac{r^a_{m2}}{s-s_{m2}} + \frac{r^a_{m3}}{s-s_{m3}}\Big), \tag{72}$$

$$G_m(s) = \frac{q}{M}\Big(\frac{r^b_{m1}}{s-s_{m1}} + \frac{r^b_{m2}}{s-s_{m2}} + \frac{r^b_{m3}}{s-s_{m3}}\Big), \tag{73}$$

where s_{m1}, s_{m2} and s_{m3} are the roots of the third-order polynomial in the denominator of Equations (70) and (71). The closed form expressions for these roots can be found in mathematical handbooks. The six coefficients r can be calculated from the equations

$$\left\{\begin{matrix} r^a_{m1} \\ r^a_{m1} \\ r^a_{m1} \end{matrix}\right\} = \left[\begin{array}{c|c|c} 1 & 1 & 1 \\ s_{m2}+s_{m3} & s_{m1}+s_{m3} & s_{m1}+s_{m2} \\ s_{m2}s_{m3} & s_{m1}s_{m3} & s_{m1}s_{m2} \end{array}\right]^{-1} \left\{\begin{matrix} C_1 \\ -\mathcal{M}^a_{10}/\mathcal{M}_1 \\ \mathcal{M}^a_{11}/\mathcal{M}_1 \end{matrix}\right\}, \tag{74}$$

$$\left\{\begin{matrix} r^b_{m1} \\ r^b_{m1} \\ r^b_{m1} \end{matrix}\right\} = \left[\begin{array}{c|c|c} 1 & 1 & 1 \\ s_{m2}+s_{m3} & s_{m1}+s_{m3} & s_{m1}+s_{m2} \\ s_{m2}s_{m3} & s_{m1}s_{m3} & s_{m1}s_{m2} \end{array}\right]^{-1} \left\{\begin{matrix} C_2 \\ -\mathcal{M}^b_{10}/\mathcal{M}_1 \\ \mathcal{M}^a_{11}/\mathcal{M}_1 \end{matrix}\right\}. \tag{75}$$

Finally, we perform an inverse Laplace transformation and obtain

$$A_m(t) = \frac{q}{M}\left(r^a_{m1}e^{s_{m1}t} + r^a_{m2}e^{s_{m2}t} + r^a_{m3}e^{s_{m3}t}\right), \tag{76}$$

$$B_m(t) = \frac{q}{M}\left(r^b_{m1}e^{s_{m1}t} + r^b_{m2}e^{s_{m2}t} + r^b_{m3}e^{s_{m3}t}\right). \tag{77}$$

The excess pressures at the two pore scales can then be obtained as

$$p_1(z,t) = \sum_{m=1}^{\infty} \frac{q}{M}\sin\left(\frac{M}{H}z\right)\left(r^a_{m1}e^{s_{m1}t} + r^a_{m2}e^{s_{m2}t} + r^a_{m3}e^{s_{m3}t}\right), \tag{78}$$

$$p_2(z,t) = \sum_{m=1}^{\infty} \frac{q}{M}\sin\left(\frac{M}{H}z\right)\left(r^b_{m1}e^{s_{m1}t} + r^b_{m2}e^{s_{m2}t} + r^b_{m3}e^{s_{m3}t}\right). \tag{79}$$

The vertical strain can be calculated by substituting the excess pore pressures into Equation (33) to obtain the effective vertical stress, and then to the elasto-viscoplastic constitutive Equation (7) to obtain

$$\varepsilon_{\mathrm{v}} = -\frac{q}{D} - \frac{q}{\mathcal{H}}\left[1-e^{-\mathcal{H}t/\eta}\right] + \sum_{m=1}^{\infty}\frac{q}{M}\sin\left(\frac{M}{H}z\right)\Big(\beta_1 g^a_m(t) + \beta_2 g^b_m(t)\Big) \tag{80}$$

with

$$g_m^a(t) = \frac{1}{D}\left(r_{m1}^a e^{s_{m1}t} + r_{m2}^a e^{s_{m2}t} + r_{m3}^a e^{s_{m3}t}\right) + \frac{r_{m1}^a}{\eta s_{m1} + \mathcal{H}}\left(e^{s_{m1}t} - e^{-\mathcal{H}t/\eta}\right) + \frac{r_{m2}^a}{\eta s_{m2} + \mathcal{H}}\left(e^{s_{m2}t} - e^{-\mathcal{H}t/\eta}\right) + \frac{r_{m3}^a}{\eta s_{m3} + \mathcal{H}}\left(e^{s_{m3}t} - e^{-\mathcal{H}t/\eta}\right), \tag{81}$$

$$g_m^b(t) = \frac{1}{D}\left(r_{m1}^b e^{s_{m1}t} + r_{m2}^b e^{s_{m2}t} + r_{m3}^b e^{s_{m3}t}\right) + \frac{r_{m1}^b}{\eta s_{m1} + \mathcal{H}}\left(e^{s_{m1}t} - e^{-\mathcal{H}t/\eta}\right) + \frac{r_{m2}^b}{\eta s_{m2} + \mathcal{H}}\left(e^{s_{m2}t} - e^{-\mathcal{H}t/\eta}\right) + \frac{r_{m3}^b}{\eta s_{m3} + \mathcal{H}}\left(e^{s_{m3}t} - e^{-\mathcal{H}t/\eta}\right). \tag{82}$$

Taking the integral of the negative strain over the depth and dividing the result by H gives the normalized settlement

$$\frac{\Delta H(t)}{H} = \frac{q}{D} + \frac{q}{\mathcal{H}}(1 - e^{-\mathcal{H}t/\eta}) - \sum_{m=1}^{\infty} \frac{q}{M^2}(1 - \cos M)\left(\beta_1 g_m^a(t) + \beta_2 g_m^b(t)\right). \tag{83}$$

Observe the similar form of this solution to Equation (28).

We recall the four characteristic time scales for a double-porosity system identified in Equation (54): τ_{h}^a, τ_{h}^b, $\tau_{\mathrm{v}1}$, and $\tau_{\mathrm{v}2}$. The first two of these four time scales are associated with the expulsion of fluid from the macropores and micropores, whereas the last two are associated with the elasto-viscoplastic response of the soil skeleton. The previous study in Section 2 reveals that the relative magnitude of $\tau_{\mathrm{v}1}$ and $\tau_{\mathrm{v}2}$ simply defines the shape of the settlement-time response (whether it is a single or double S-shaped curve), which is the same result for the double-porosity system. Therefore, in the following analyses we shall only focus on the three time scales: τ_{h}^a, τ_{h}^b, and $\tau_{\mathrm{v}1}$.

For a double porosity system, a few other variables such as N, β and γ could influence the time-dependent response. The variables that have the greatest influence on the system response are the coefficients $N_1 = D/m_1$ and $N_2 = D/m_2$, which depend on the elastic constrained modulus D of the soil skeleton and the Biot moduli m_1 and m_2. Thus, we will group the following presentation according to the values of these variables.

3.1 Low D/m moduli ratio

The coefficient $N_i = D/m_i$, which represents the ratio between the constrained bulk modulus D of the soil skeleton and the Biot modulus m_i for pore scale i, determines the effective vertical stress initially carried by the soil skeleton as a result of the applied surface load q. If this ratio is close to zero, then $N_i \ll \beta_i$ and

$$C_3 = \frac{N_1 N_2}{N_1 N_2 + N_2 \beta_1^2 + N_1 \beta_2^2} \approx 0, \tag{84}$$

which means that all of the load is carried by the excess pore pressures at $t = 0^+$ and none of the load is carried by the effective stress in the soil skeleton. In addition, the ratios

$$\mathrm{O}\left(\frac{\mathcal{M}_1}{\mathcal{M}_2}\right) = \mathrm{O}\left(\frac{N_i \tau_{\mathrm{h}}^a}{M^2}\right) \tag{85}$$

appearing in Equations (70) and (71) are small, implying that even though the denominators for $F_m(s)$ and $G_m(s)$ are in the form of a cubic polynomial, they can be approximated by quadratic polynomials like the one considered in Section 2. Next we set $\mathcal{H} = D$ so that $\tau_{\mathrm{v}1} = \tau_{\mathrm{v}2} := \tau_{\mathrm{v}}$ and assume $\beta_1 = \beta_2 = 0.5$ to reduce the number of variables. Defining $\gamma = k_2 D/\rho_{\mathrm{w}} g$ using the formula

$$c_1 = \frac{\bar{\alpha}}{\mu}(p_2 - p_1) = \frac{\gamma}{D}(p_2 - p_1) \tag{86}$$

provided in [13], and setting

$$\bar{\alpha} = \kappa_2 = \frac{\mu k_2}{\rho_{\mathrm{w}} g}\,, \tag{87}$$

we can then investigate how τ_{h}^a, τ_{h}^b and τ_{v} affect the resulting settlement-time responses.

To investigate the resulting settlement-time responses, we first fix the time scales at $\tau_{\mathrm{h}}^a = 10$ s and $\tau_{\mathrm{v}} = 10^8$ s and vary τ_{h}^b from 10^4 to 10^{10} s by changing the hydraulic conductivity k_2 of the micropores. Defining

$$c^b = \frac{\tau_{\mathrm{h}}^b}{\tau_{\mathrm{v}}} = \frac{H^2}{c_{\mathrm{v}2}} \frac{\mathcal{H}}{\eta}\,, \tag{88}$$

the corresponding consolidation curves are plotted in Figure 5. We see that for small c^b the double S-shaped consolidation curves are very distinct, implying that the dissipation of excess pore pressure is completed well before the significant development of viscoplastic strain in the soil skeleton. The duration of the consolidation is determined by τ_{v}, and an increase of τ_{h}^b only increases the duration of the first stage of settlement. However, as τ_{h}^b further increases to a value greater than τ_{v}, the pore pressure dissipation effect begins to cover the viscoplastic stage of settlement. Eventually, the curve reduces to a single S shape with the duration determined by τ_{h}^b. This trend is comparable to that reported in Figure 4.

We next investigate the effect of τ_{h}^a by fixing the remaining time scales at $\tau_{\mathrm{h}}^b = 10^6$ s and $\tau_{\mathrm{v}} = 10^8$ s, thus fixing c^b at the value 10^{-2}. From Figure 6, we see that the ratio

$$c^a = \frac{\tau_{\mathrm{h}}^a}{\tau_{\mathrm{v}}} = \frac{H^2}{c_{\mathrm{v}1}} \frac{\mathcal{H}}{\eta} \tag{89}$$

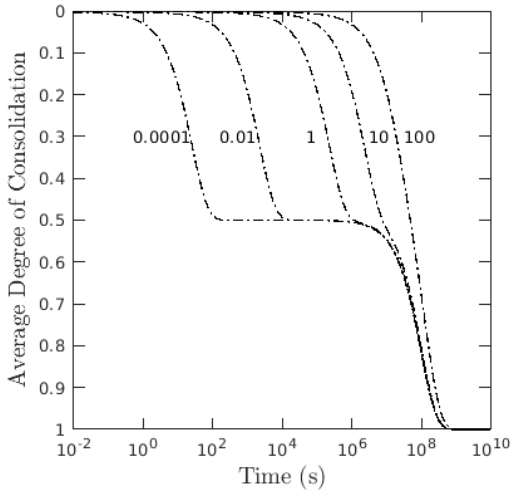

Fig. 5. Variation of average degree of consolidation with c^b.

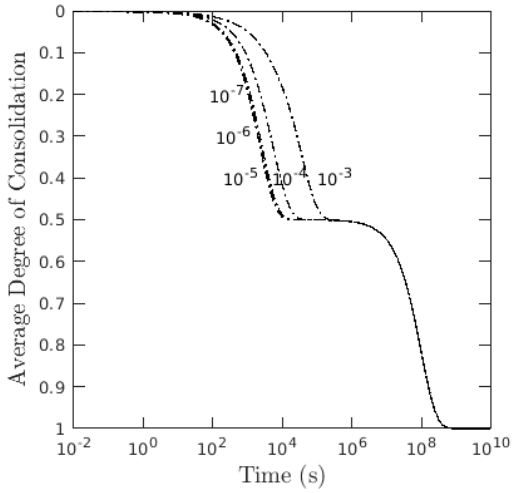

Fig. 6. Variation of average degree of consolidation with c^a.

has a negligible influence on the settlement-time curve when it is at least two orders of magnitude smaller than c^b. Only when the hydraulic conductivity of the macropores k_1 becomes small enough and the time scale τ_{h}^a becomes comparable to the time scale τ_{h}^b does the primary settlement curve begin to shift to the right. On the other hand, we know that the hydraulic conductivity of the macropores is typically much greater than that of the micropores, so we conclude that c^a does not have a significant impact on the settlement-time

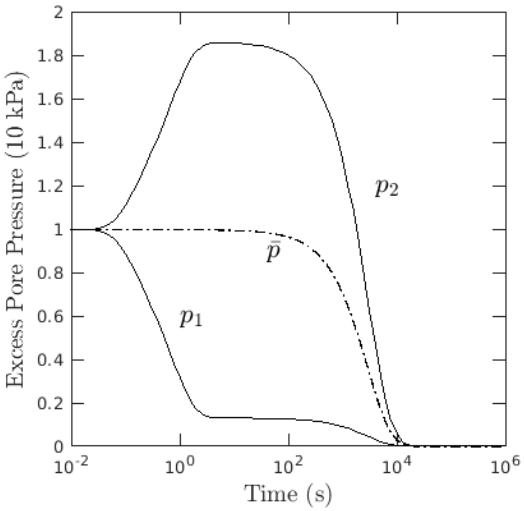

Fig. 7. Time-histories of excess pore pressures for $\tau_{\mathrm{h}}^{a} = 10^{3}$ and $\tau_{\mathrm{h}}^{b} = 10^{6}$ s.

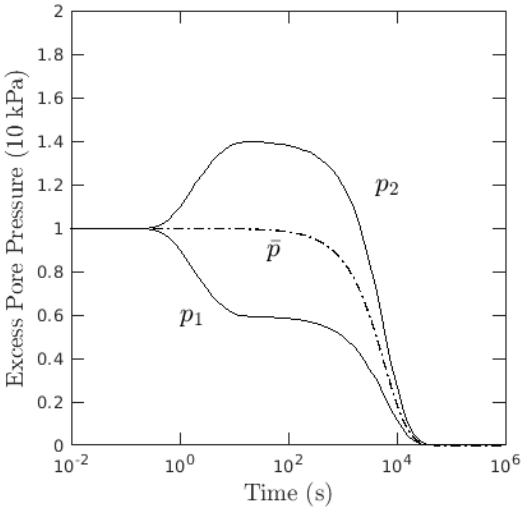

Fig. 8. Time-histories of excess pore pressures for $\tau_{\mathrm{h}}^{a} = 10^{4}$ s and $\tau_{\mathrm{h}}^{b} = 10^{6}$ s.

curve. This implies that the hydrodynamic properties of the double-porosity system is dominated by the hydrodynamic properties of the micropores.

Nevertheless, c^{a} can still impact the time-histories of the excess pore pressures in the macropores and micropores. Figures 7 and 8 show the time-histories of p_1, p_2, and the mean excess pore pressure $\bar{p} = \beta_1 p_1 + \beta_2 p_2$ at a

depth of $z = H/2$ for the double-porosity system. In these figures, the time scale τ_{h}^{b} was fixed at 10^6 s while τ_{h}^{a} was assigned two different values, namely, 10^3 and 10^4 s.

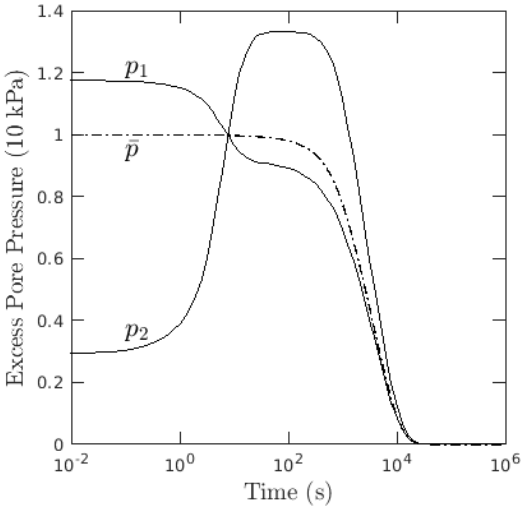

Fig. 9. Time-histories of excess pore pressures for $\beta_1 = 0.8$ and $\beta_2 = 0.2$.

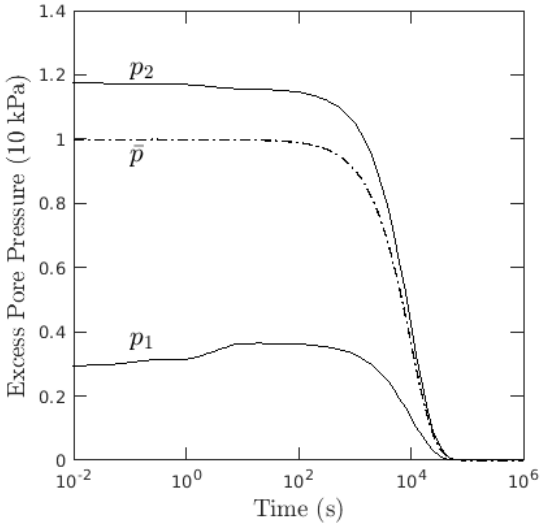

Fig. 10. Time-histories of excess pore pressures for $\beta_1 = 0.2$ and $\beta_2 = 0.8$.

The two figures show that the evolution of the excess pore pressures can be separated into three stages. In the first stage, the excess pore pressure decreases in the macropores but increases in the micropores. Both excess pore pressures plateau in the second stage. In the third stage, the two excess pressures decrease, but the decrease in the micropore pressure is faster. The beginning and end of the first stage are determined by τ_{h}^{a}. Furthermore, the pressure drop in the macropores and the pressure rise in the micropores increase with τ_{h}^{a}. On the other hand, the beginning and end of the third stage are determined by τ_{h}^{b}, while the duration of the second stage is determined by the difference between τ_{h}^{a} and τ_{h}^{b}. In any case, the mean pressure $\bar{p}$ remains constant during the first and second stages, and only decreases during the third stage. Since the effective vertical stress is determined by $\bar{p}$, we again conclude that the settlement-time history is not affected by τ_{h}^{a}.

We have previously mentioned that the coefficients β_1 and β_2 also affect the initial solutions for the excess pore pressures. When the macropores occupy most of the pore spaces like the case shown in Figure 9, we see that the initial excess pore pressure in the macropores is higher than in the micropores. However, when the micropores occupy most of the pore spaces like the case shown in Figure 10, the initial excess pore pressures in the micropores is higher. Regardless of which pore scale occupies more pore space, we always see three stages in the pressure histories, but the mean excess pore pressure $\bar{p}$ remains unaffected by the values of β_1 and β_2.

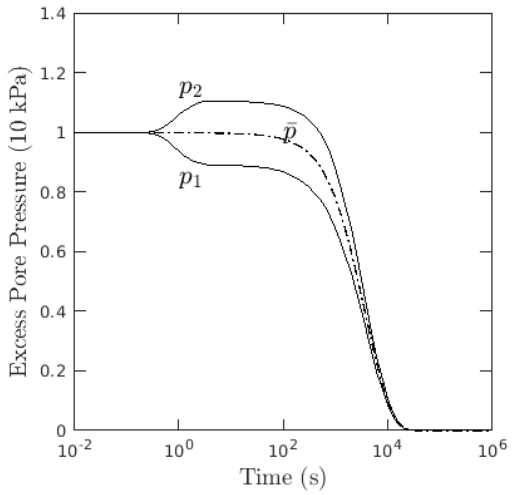

Fig. 11. Time-histories of excess pore pressures for $\gamma = 5k_2D/\rho_{\mathrm{w}}g$.

Finally, we investigate the effect of parameter γ in Figure 11. When this parameter is increased five times than the value used in Figure 8, we see that

the fluid exchange efficiency at the two pore scales is improved, effectively homogenizing the excess pore pressures. In other words, both p_1 and p_2 approach the mean excess pore pressure $\bar{p}$. However, neither $\bar{p}$ nor the settlement-time history is affected by γ.

3.2 High D/m moduli ratio

For hard geomaterials such as rock, the value of the coefficient N_i is comparable to β_i, and so, C_3 can no longer be neglected. This means that an initial effective vertical stress due to the applied load q will develop in the soil skeleton, resulting in an instantaneous settlement at $t = 0^+$. In addition, the coefficient $\mathcal{M}_1$ in Equations (70) and (71) can no longer be neglected. In the following examples, we show that for hard geomaterials, γ becomes an important parameter of the solution.

We first consider a large value of γ on the order of $100k^*D/\rho_{\mathrm{w}}g$, where $k^* = 10^{-7}$ m/s. We also assume $B = 0.8$ and set $\beta_1 = \beta_2 = 0.4$ so that the pore fractions of the two pore scales are the same. We first vary τ_{h}^b by varying the hydraulic conductivity k_2 across a range centered about k^* in the log scale while holding the following time scales fixed: $\tau_{\mathrm{h}}^a = 1$ s and $\tau_{\mathrm{v1}} = 10^8$ s. Figure 12 shows that the resulting settlement-time curves are insensitive to the values of c^b. Next we fix $\tau_{\mathrm{h}}^b = 10^4$ s and vary τ_{h}^a. Figure 13 shows that c^a now shifts the position of the primary settlement stage. This parametric study means that for hard geomaterials and large values of γ, the hydrodynamic properties of the double porosity system is influenced by the hydrodynamic properties of the macropores.

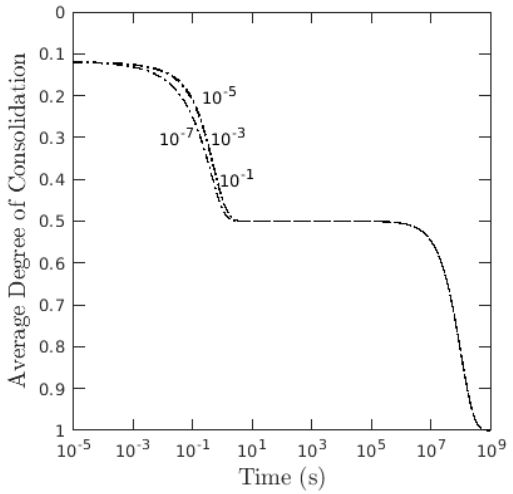

Fig. 12. Variation of average degree of consolidation with c^b for large values of γ.

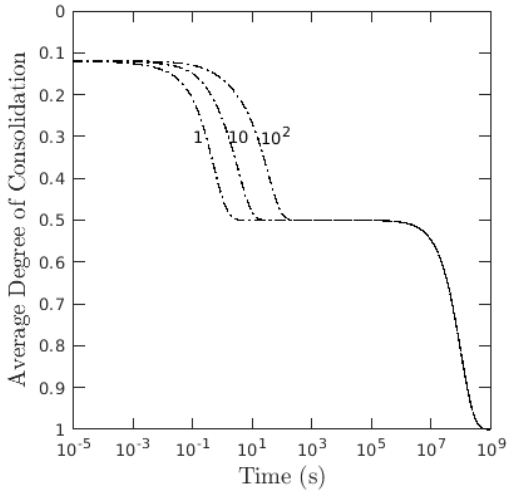

Fig. 13. Variation of average degree of consolidation with c^a for large values of γ.

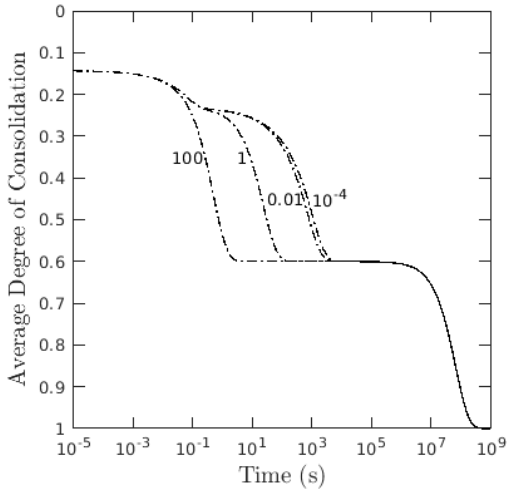

Fig. 14. Variation of average degree of consolidation with $\gamma/c_{\mathrm{v}2}$.

Next, we assume different values of γ and observe the resulting system response. To this end, we fix the three time scales at $\tau_{\mathrm{h}}^a = 1$ s, $\tau_{\mathrm{h}}^a = 10^4$ s, and $\tau_{\mathrm{v}1} = 6.7 \times 10^7$ s. For better visualization, we select an $\mathcal{H}/D$ ratio of 1.5, although the results do not really depend much on the value of this ratio. We see from Figure 14 that when γ is large, only two settlement stages can

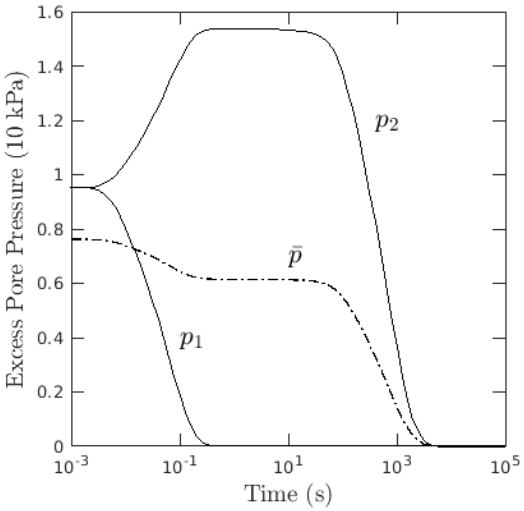

Fig. 15. Time-histories of excess pore pressures for $\gamma = 0.01 c_{\mathrm{v}2}$.

be identified from the settlement-time curve, one characterized by τ_{h}^a and the other by $\tau_{\mathrm{v}1}$. However, as the value of γ is reduced, a third (intermediate) settlement stage emerges with a characteristic time scale somewhere between τ_{h}^a and τ_{h}^b. As the value of γ is reduced further and approaches the value $0.01 c_{\mathrm{v}2}$, the time scale approaches τ_{h}^b, and decreasing γ further no longer affects the system response.

Figure 15 shows how γ impacts the excess pore pressure variations in the double-porosity medium. We see that the mean excess pore pressure $\bar{p}$ decreases in two steps, first following the drop in p_1, and then following the drop in p_2. This is unique to this solution in that previous simulations showed $\bar{p}$ remaining essentially steady despite the wild variations in p_1 and p_2 until it begins to decrease. The pressure-time history shown in Figure 15 demonstrates that $\bar{p}$ could also be influenced by the excessive variations of the fluid pressures in the two pore scales.

Finally, Figure 16 shows the effect of β_1 and β_2 on the settlement-time curve. The first S-shaped curve signifies primary compression of the macropes; the second S-shaped curve is the secondary compression of the micropores; the third S-shaped curve is the additional compression due to viscoplastic creep. Note that larger β_1 means higher macropore fraction and greater settlement as the excess macropore pressure dissipates.

3.3 Summary of main points

For a double-porosity system, the primary compression is attributed to pore pressure dissipation. Depending on the moduli ratio D/m, the secondary com-

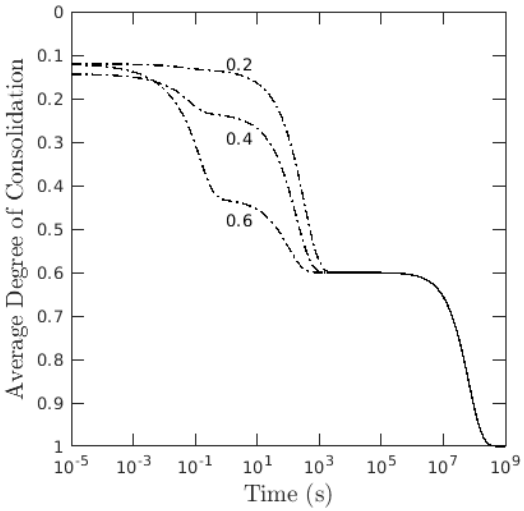

Fig. 16. Variation of average degree of consolidation with β_1 (note: $\beta_2 = 0.8 - \beta_1$).

pression is attributed to either the elasto-viscoplastic deformation of the soil skeleton alone, or the combined effect of fluid discharge from the micropores to the macropores or outside the system, followed by the elasto-viscoplastic deformation of the soil skeleton. Four characteristic time scales exist for both cases, namely, τ_{h}^{a}, τ_{h}^{b}, $\tau_{\mathrm{v}1}$ and $\tau_{\mathrm{v}2}$, but the first three time scales are sufficient to characterize the settlement-time history of the system.

For soft geomaterials where the moduli ratio D/m is small, the behavior of the system is very close to that of a single-porosity system where the settlement-time history may exhibit one or two stages of deformation across the time scale. For hard geomaterials where D/m is large, the behavior of the system is sensitive to the value of the coefficient γ related to the fluid exchange at the two pore scales. When γ is large, the hydrodynamic properties of the system are dominated by those of the macropores. However, when γ is small, the system response depends on the hydrodynamic properties of both the macropores and micropores. In the latter case, the first three time scales can produce a settlement-time history exhibiting three stages of deformation across the time scale.

4 Time scale in Bjerrum's creep model

Creep is a time-dependent deformation that takes place under a condition of sustained load. If the vertical effective stress σ'_{v} is constant, then the viscoplastic strain predicted in Equation (5) becomes the creep strain, i.e.,

$$\varepsilon^{\mathrm{cr}} = \varepsilon^{\mathrm{vp}}|_{\sigma'_{\mathrm{v}}=\mathrm{const}} = \frac{\sigma'_{\mathrm{v}}}{\eta}\int_0^t e^{-\mathcal{H}(t-\tau)/\eta}\,\mathrm{d}\tau = \frac{\sigma'_{\mathrm{v}}\tau_{\mathrm{v1}}}{\eta}(1-e^{-t/\tau_{\mathrm{v1}}})\,, \tag{90}$$

where $\tau_{\mathrm{v1}} = \eta/\mathcal{H}$ is the characteristic viscoplastic time scale defined in Section 2. We recall that σ'_{v} is the full over-stress value in Equation (5) from the assumption that $\sigma_{\mathrm{Y0}} = 0$. Furthermore, $\varepsilon^{\mathrm{cr}} \to \sigma'_{\mathrm{v}}\tau_{\mathrm{v1}}/\eta$ as $t \to \infty$, which means that there is a finite long-term creep strain that develops in the soil. We can view this long-term creep strain as developing at an average rate of $\sigma'_{\mathrm{v}}/\eta$ and having a duration of τ_{v1}, thus providing a further physical meaning for this time scale.

We now differentiate the above viscoplastic model with the phenomenological creep model proposed by Bjerrum [8]. Under one-dimensional consolidation, Bjerrum identified parallel straight lines on the void ratio-logarithm of effective vertical stress plane and associated each line with a certain "age" of the soil sample. Borja and Kavazanjian [18] referred to this age as "volumetric age" to distinguish it from "deviatoric age" that characterizes the straight lines constructed from undrained triaxial creep tests [67]. If the volumetric age of one of the straight lines is 10 times larger than the volumetric age of the straight line above it, then the parallel lines will be equidistant from each other. This means that the vertical creep strain (equal to the volumetric creep strain under 1D constrained condition) can be expressed as a logarithmic function of the volumetric age, i.e.,

$$\varepsilon^{\mathrm{cr}} = \varepsilon_0^{\mathrm{cr}} - c_\alpha \log_{10}\left(\frac{t}{t_0}\right), \tag{91}$$

where $\varepsilon_0^{\mathrm{cr}}$ is the creep strain at reference time t_0 and c_α is a secondary compression coefficient characterizing the creep response of the soil. Since $\varepsilon^{\mathrm{cr}} \to -\infty$ as $t \to \infty$, Bjerrum's model predicts that the soil will creep indefinitely. This implies that the time scale in Bjerrum's creep model is infinity.

An upshot of the above result is that, when combined with hydrodynamic lag, Bjerrum's creep model predicts only one S-shaped curve on the settlement versus logarithm-of-time response due to primary consolidation, followed by a straight-line tail due to secondary consolidation. We present a numerical example to illustrate this point below. In this example, the following parameters of the soil were obtained from Borja and Kavazanjian [18] for an overconsolidated clay: recompression index $\kappa = 0.054$ and secondary compression coefficient $c_\alpha = 0.0065$. Figure 17 shows the settlement-time history responses for three values of hydraulic conductivity. Two different stages of settlement can be observed from the curves: an S-shaped curve characterizing the primary consolidation stage, and a straight-line tail characterizing the secondary consolidation stage. All curves converge to the same secondary consolidation line at the completion of the primary consolidation.

To conclude, the primary-secondary consolidation behavior of a soil modeled with Bjerrum's phenomenological creep theory exhibits two stages of settlement. The primary settlement is determined by the hydrodynamic prop-

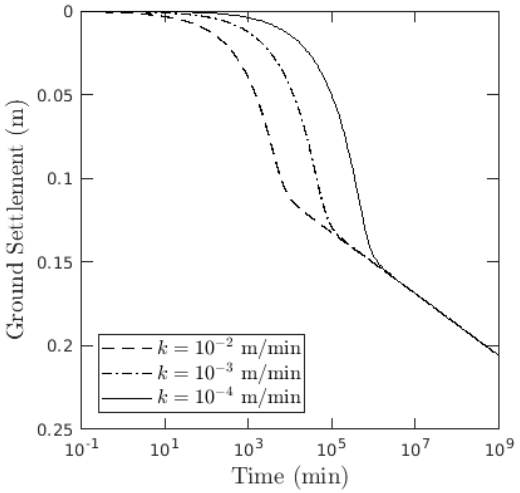

Fig. 17. Variation of ground settlement with k for an overconsolidated clay. See Borja and Kavazanjian [18] for a full formulation of the model.

erties of the system and has an associated time scale that is inversely proportional to the hydraulic conductivity of the system. The secondary settlement represents the creep deformation that accumulates without limit and has no finite time scale.

5 Closure

We have presented analytical solutions to the problem of combined primary and secondary compression of soils in one dimension considering different secondary compression processes and the associated time scales. For a single-porosity system or a double-porosity system with a low D/m moduli ratio, the relevant processes include the dissipation of excess pore pressure either in the pore spaces for a single-porosity system or in the micropores for a double-porosity system, and the viscoplastic deformation of the soil skeleton. For a double-porosity system with a high D/m ratio, the fluid transfer efficiency between the two pore scales determines the overall system response. Finally, when combined with the primary consolidation process, Bjerrum's phenomenological creep model does not exhibit a finite time scale and only the time scale associated with the primary compression can be identified.

Acknowledgments

Support for this work was provided by the National Science Foundation under Award Number CMMI-1914780.

Data availability statement

The datasets generated during the course of this study are available from the corresponding author upon reasonable request.

References

[1] Abousleiman YA, Cheng AH-D, Jiang C, Roegiers JC (1996). Poroviscoelastic analysis of borehole and cylinder problems. Acta Mechanica 119: 199–219.
[2] Alexandre G, Martins I (2014). An Interpretation of Secondary Consolidation for the Batiscan Clay.
[3] Baligh MM, Levadoux JN (1978). Consolidation theory for cyclic loading. Journal of the Geotechnical Engineering Division 104(4):415–431.
[4] Barbour SL, Fredlund DG (1989). Mechanisms of osmotic flow and volume change in clay soils. Canadian Geotechnical Journal 26(4):551–562.
[5] Barden L (1965). Consolidation of clay with non-linear viscosity. Géotechnique 15(4):345–362.
[6] Barden L (1969). Time dependent deformation of normally consolidated clays and peats. Journal of the Soil Mechanics and Foundations Division 95(1):1–31.
[7] Bergins C (2004). Mechanical/thermal dewatering of lignite. Part 2: A rheological model for consolidation and creep process. Fuel 83(3):267–276.
[8] Bjerrum L (1967). Engineering geology of Norwegian normally-consolidated marine clays as related to settlements of buildings. Géotechnique 17:81–118.
[9] Bolt GH (1956). Physico-chemical analysis of the compressibility of pure clays. Géotechnique 6(2):86–93.
[10] Booker JR, Small JC (1987). A method of computing the consolidation behaviour of layered soils using direct numerical inversion of Laplace transforms. International Journal for Numerical and Analytical Methods in Geomechanics 11(4):363–380.
[11] Borja RI (2022). Computational Poromechanics. Lecture Notes, Stanford University, USA.
[12] Borja RI, Yin Q, Zhao Y (2020). Cam-Clay plasticity. Part IX: On the anisotropy, heterogeneity, and viscoplasticity of shale. Computer Methods in Applied Mechanics and Engineering 360:112695.

[13] Borja RI, Choo J (2016). Cam-Clay plasticity, Part VIII: A constitutive framework for porous materials with evolving internal structure. Computer Methods in Applied Mechanics and Engineering 309:653–679.
[14] Borja RI (2013). Plasticity Modeling & Computation. Springer, Berlin-Heidelberg.
[15] Borja RI, Koliji A (2009). On the effective stress in unsaturated porous continua with double porosity. Journal of the Mechanics and Physics of Solids 57(8):1182–1193
[16] Borja RI (2006). On the mechanical energy and effective stress in saturated and unsaturated porous continua. International Journal of Solids and Structures 43(6):1764–1786.
[17] Borja RI (1992). Generalized creep and stress relaxation models for clays. Journal of Geotechnical Engineering 118(11), 1992:1765–1786.
[18] Borja RI, Kavazanjian E (1985). A constitutive model for the stress-strain-time behaviour of 'wet' clays. Géotechnique 35(3):283–298.
[19] Bowman ET, Soga K (2003). Creep, ageing and microstructural change in dense granular materials. Soils and foundations 43(4):107–117.
[20] Camargo JT, White JA, Castelletto N, Borja RI (2021). Preconditioners for multiphase poromechanics with strong capillarity. International Journal for Numerical and Analytical Methods in Geomechanics 45(9):1141–1168.
[21] Chang C, Mallman E, Zoback M (2014). Time-dependent subsidence associated with drainage-induced compaction in Gulf of Mexico shales bounding a severely depleted gas reservoir. AAPG Bulletin 98(6):1145–1159.
[22] Cheng AHD, Sidauruk P, Abousleiman Y (1994). Approximate inversion of the Laplace transform. The Mathematical Journal 4(2):76–82.
[23] Choo J, Borja RI (2015). Stabilized mixed finite elements for deformable porous media with double porosity. Computer Methods in Applied Mechanics and Engineering 293:131–154.
[24] Choo J, White JA, Borja RI (2016). Hydromechanical modeling of unsaturared flow in double porosity media. International Journal of Geomechanics 16(6), doi.org/10.1061/(ASCE)GM.1943-5622.0000558.
[25] Cosenza P, Korošak D (2014). Secondary consolidation of clay as an anomalous diffusion process. International Journal for Numerical and Analytical Methods in Geomechanics 38(12):1231–1246.
[26] Crawford CB (1964). Interpretation of the consolidation test. Journal of the Soil mechanics and Foundations Division 90(5): 87–102.
[27] Davis EH, Raymond GP (1965). A non-linear theory of consolidation. Géotechnique, 15(2):161–173.
[28] De Jong GDJ (1968). Consolidation models consisting of an assembly of viscous elements or a cavity channel network. Géotechnique 18(2):195–228.

[29] De Waal JA, Smits RMM (1988). Prediction of reservoir compaction and surface subsidence: Field application of a new model. SPE Formation Evaluation 3(02):347–356.
[30] Fredlund DG, Hasan JU (1979). One-dimensional consolidation theory: unsaturated soils. Canadian Geotechnical Journal 16(3):521–531.
[31] Favaretti M, Soranzo M (1995). A simplified consolidation theory in cyclic loading conditions. Compression and consolidation of clayey soils:405–409.
[32] Feda J (1992). Creep of Soils: and Related Phenomena. Elsevier.
[33] Fernandes MM (2020). Analysis and design of geotechnical structures. CRC Press.
[34] Flügge W (1975). Viscoelasticity, Second Revised Edition, Springer-Verlag, Berlin Heidelberg.
[35] Gray H (1936). Progress report on research on the consolidation of fine-grained soils. First International Conference on Soil Mechanics and Foundation Engineering 2:138–141.
[36] Hameedi MK, Al Omari RR, Fattah MY (2020). Compression and creep indices of organic clayey soil. IOP Conference Series: Materials Science and Engineering 671(1):012035.
[37] Ho L, Fatahi B (2016). One-dimensional consolidation analysis of unsaturated soils subjected to time-dependent loading. International Journal of Geomechanics 16(2):04015052.
[38] Hoang SK, Abousleiman YN (2010). Poroviscoelasticity of transversely isotropic cylinders under laboratory loading conditions. Mechanics Research Communications 37(3):298–306.
[39] Ip SCY, Choo J, Borja RI (2022). Impacts of saturation-dependent anisotropy on the shrinkage behavior of clay rocks. Acta Geotechnica 16(11):3381–3400.
[40] Ip SCY, Borja RI (2022). Evolution of anisotropy with saturation and its implications for the elastoplastic responses of clay rocks. International Journal for Numerical and Analytical Methods in Geomechanics 46(1):23–46.
[41] Kavazanjian E, Mitchell JK (1980). Time-dependent deformation behavior of clays. Journal of the Geotechnical Engineering Division, ASCE 106(6):611–630.
[42] Kuhn MR, Mitchell JK (1993). New perspectives on soil creep. Journal of Geotechnical Engineering 119(3):507–524.
[43] Lee PKK, Xie KH, Cheung YK (1992). A study on one-dimensional consolidation of layered systems. International Journal for Numerical and Analytical Methods in Geomechanics 16(11): 815–831.
[44] Leroueil S, Kabbaj M, Tavenas F, Bouchard R (1985). Stress–strain–strain rate relation for the compressibility of sensitive natural clays. Géotechnique, 35(2):159–180.

[45] Lewallen KT, Wang HF (1998). Consolidation of a double-porosity medium. International Journal of Solids and Structures 35(34–35):4845–4867.

[46] Lewis RW, Tran DV (1989). Numerical simulation of secondary consolidation of soil: Finite element application. International Journal for Numerical and Analytical Methods in Geomechanics 13(1):1–18.

[47] Li L, Qin A, Jiang L (2021). Semi-analytical solution for one-dimensional consolidation of a two-layered soil system with unsaturated and saturated conditions. International Journal for Numerical and Analytical Methods in Geomechanics 45(15):2284–2300.

[48] Liu C, Hoang SK, Tran MH, Abousleiman YN, Ewy RT (2017). Poroelastic dual-porosity dual-permeability simulation of pressure transmission test on chemically active shale. Journal of Engineering Mechanics 143(6): 04017016.

[49] Lloret A, Alonso EE (1980). Consolidation of unsaturated soils including swelling and collapse behaviour. Géotechnique 30(4):449–477.

[50] Lo WC, Borja RI, Deng J-H, Lee J-W (2020). Analytical solution of soil deformation and fluid pressure change for a two-layer system with an upper unsaturated soil and a lower saturated soil under external loading. Journal of Hydrology 588:124997.

[51] Lo WC, Chang JC, Borja RI, Deng J-H, Lee J-W (2021). Mathematical modeling of consolidation in unsaturated poroelastic soils under fluid flux boundary conditions. Journal of Hydrology 595: 125671.

[52] Lo WC, Borja RI, Deng J-H, Lee J-W (2021). Poroelastic theory of consolidation for a two-layer system with an upper unsaturated soil and a lower saturated soil under fully permeable boundary conditions. Journal of Hydrology 596:125700.

[53] Mánica MA, Gens A, Ovando-Shelley E, Botero E, Vaunat J (2021). An effective combined framework for modelling the time-dependent behaviour of soft structured clays. Acta Geotechnica 16:535–550.

[54] Mesri G, Godlewski PM (1977). Time- and stress-compressibility relationship. Journal of the Geotechnical Engineering Division, ASCE 103(5):427–430.

[55] Niemunis A, Krieg S (1996). Viscous behaviour of soil under oedometric conditions. Canadian Geotechnical Journal 33(1):159–168.

[56] Niu J, Ling D, Zhu S, Gong S, Shan Z (2021). Solutions for one-dimensional consolidation of unsaturated soil with general boundary conditions subjected to time-dependent load. International Journal for Numerical and Analytical Methods in Geomechanics 45(11):1664–1680.

[57] Olson RE (1977). Consolidation under time dependent loading. Journal of the Geotechnical Engineering Division 103(1): 55–60.

[58] Pariseau WG (1999). Poroelastic-plastic consolidation–analytical solution. International Journal for Numerical and Analytical Methods in Geomechanics 23(7):577–594.

[59] Perzyna P (1966). Fundamental problems in viscoplasticity. Advances in Applied Mechanics 9:243–377
[60] Qin AF, Chen GJ, Tan YW, Sun DA (2008). Analytical solution to one-dimensional consolidation in unsaturated soils. Applied mathematics and mechanics 29(10):1329–1340.
[61] Poskitt TJ (1969). The consolidation of saturated clay with variable permeability and compressibility. Géotechnique 19(2):234–252.
[62] Pyrah IC (1996). One-dimensional consolidation of layered soils. Géotechnique 46(3):555–560.
[63] Salomoni VA, Schrefler BA (2006). Stabilized-coupled modelling of creep phenomena for saturated porous media. International Journal for Numerical Methods in Engineering 66:1587–1617.
[64] Schiffman RL (1958). Consolidation of soil under time-dependant loading and varying permeability. Highway Research Board Proceedings 37:584–617.
[65] Schiffman RL, Stein JR (1970). One-dimensional consolidation of layered systems. Journal of the Soil Mechanics and Foundations Division 96(4):1499–1504.
[66] Shirato M, Murase T, Iwata M, Nakatsuka S (1986). The Terzaghi-Voigt combined model for constant-pressure consolidation of filter cakes and homogeneous semi-solid materials. Chemical Engineering Science 41(12):3213–3218.
[67] Singh A, Mitchell JK (1968). General stress-strain-time function for soils. Journal of the Soil Mechanics and Foundations Division, ASCE 94(1):21–46.
[68] Sridharan A, Rao AS (1982). Mechanisms controlling the secondary compression of clays. Géotechnique 32(3):249–260.
[69] Sridharan A, Rao GV (1973). Mechanisms controlling volume change of saturated clays and the role of the effective stress concept. Géotechnique 23(3):359–382.
[70] Šuklje, L. (1957). The analysis of the consolidation process by the isotaches method. In Proc. 4th ICSMFE (Vol. 1, pp. 200–206).
[71] Tian Y, Wu W, Jiang G, El Naggar MH, Mei G, Xu M, Liang R. (2020). One-dimensional consolidation of soil under multistage load based on continuous drainage boundary. International Journal for Numerical and Analytical Methods in Geomechanics 44(8):1170–1183.
[72] Wahls HE (1962). Analysis of primary and secondary consolidation. Journal of the Soil Mechanics and Foundations Division 88(6):207–231.
[73] Wilson NE, Elgohary MM (1974). Consolidation of soils under cyclic loading. Canadian Geotechnical Journal 11(3):420–423.
[74] Wilson RK, Aifantis EC (1982). On the theory of consolidation with double porosity. International Journal of Engineering Science 20(9):1009–1035.

[75] Xie KH, Xie XY, Jiang W (2002). A study on one-dimensional nonlinear consolidation of double-layered soil. Computers and Geotechnics 29(2):151–168.

[76] Xie KH, Xie XY, Li XB (2008). Analytical theory for one-dimensional consolidation of clayey soils exhibiting rheological characteristics under time-dependent loading. International Journal for Numerical and Analytical Methods in Geomechanics 32(14):1833–1855. 48(6):1011-1020.

[77] Yang X, Zong M, Tian Y, Jiang G, El Naggar MH, Wu W, Xu M. (2021). One-dimensional consolidation of layered soils under ramp load based on continuous drainage boundary. International Journal for Numerical and Analytical Methods in Geomechanics 45(6):738–752.

[78] Yao Z, Chen Z, Fang X, Wang W, Li W, Su L (2020). Elastoplastic damage seepage-consolidation coupled model of unsaturated undisturbed loess and its application. Acta Geotechnica 15(6):1637–1653.

[79] Yin J-H, Graham Y (1996). Elastic visco-plastic modelling of one-dimensional consolidation. Géotechnique 46(3):515–527.

[80] Yin Q, Liu Y, Borja RI (2021). Mechanisms of creep in shale from nanoscale to specimen scale. Computers and Geotechnics 136:104138.

[81] Zeevaert L (1986). Consolidation in the intergranular viscosity of highly compressible soils. In: FC Townsend (Ed.) Consolidation of Soils: Testing and Evaluation, ASTM International.

[82] Zhang H, Lu M, Zheng Y, Zhang S (2015). General coupling extended multiscale FEM for elasto-plastic consolidation analysis of heterogeneous saturated porous media. International Journal for Numerical and Analytical Methods in Geomechanics 39(1):63-95.

[83] Zhang Q, Choo J, Borja RI (2019). On the preferential flow patterns induced by transverse isotropy and non-Darcy flow in double porosity media. Computer Methods in Applied Mechanics and Engineering 353:570–592.

[84] Zhang Q, Borja RI (2020). Poroelastic coefficients for anisotropic single and double porosity media. Acta Geotechnica 16(10):3013–3025.

[85] Zhao Y, Borja RI (2021). Anisotropic elastoplastic response of double-porosity media. Computer Methods in Applied Mechanics and Engineering 380:113797.

[86] Zhao Y, Borja RI (2020). A continuum framework for coupled solid deformation-fluid flow through anisotropic elastoplastic porous media. Computer Methods in Applied Mechanics and Engineering 369:113225.

[87] Zhao X, Ng CW, Zhang S, Ni J, Zhou C (2020). An explicit one-dimensional consolidation solution with semi-permeable drainage boundary for unsaturated soil. International Journal for Numerical and Analytical Methods in Geomechanics 44(16):2241–2253.

[88] Zhou F, Wang L, Liu H. (2021). A fractional elasto-viscoplastic model for describing creep behavior of soft soil. Acta Geotechnica 16(1):67–76.

[89] Zhou WH, Zhao LS, Li XB (2014). A simple analytical solution to one-dimensional consolidation for unsaturated soils. International Journal for Numerical and Analytical Methods in Geomechanics 38(8):794–810.

[90] Zou SF, Li JZ, Xie XY (2018). A semi-analytical solution for one-dimensional elasto-viscoplastic consolidation of layered soft clay. Applied Clay Science 153:9–15.